Passive radar imaging of ship targets with GNSS signals of opportunity

Pastina, Debora; Santi, Fabrizio; Pieralice, Federica; Antoniou, Michail; Cherniakov, Mike

DOI:
10.1109/TGRS.2020.3005306

Passive radar imaging of ship targets with GNSS signals of opportunity

Debora Pastina, Fabrizio Santi, Federica Pieralice, Michail Antoniou, Mikhail Cherniakov

Abstract—**This paper explores the possibility to exploit GNSS signals to obtain radar imagery of ships. This is a new application area for the GNSS remote sensing, which adds to a rich line of research about the alternative utilization of navigation satellites for remote sensing purposes, which currently includes reflectometry, passive radar and SAR systems. In the field of short-range maritime surveillance, GNSS-based passive radar has already proven to detect and localize ship targets of interest. The possibility to obtain meaningful radar images of observed vessels would represent an additional benefit, opening the doors to non-cooperative ship classification capability with this technology. To this purpose, a proper processing chain is here conceived and developed, able to achieve well-focused images of ships while maximizing their signal-to-background ratio. Moreover, the scaling factors needed to map the backscatter energy in the range & cross-range domain are also analytically derived, enabling the estimation of the length of the target. The effectiveness of the proposed approach at obtaining radar images of ship targets and at extracting relevant features is confirmed via an experimental campaign, comprising multiple Galileo satellites and a commercial ferry undergoing different kinds of motion.**

Keywords— Passive radar imaging, GNSS-based passive radar, feature extraction, maritime surveillance.

I. INTRODUCTION

THE re-use of Global Navigation Satellite Systems (GNSS) for remote sensing applications has been studied for nearly three decades. Since the early 1990s, the analysis of GNSS signals reflected from the Earth' surface (GNSS-Reflectometry, GNSS-R) has brought to a number of innovative remote sensing applications. One of the first examples is the ESA's Passive Reflectometry and Interferometry System (PARIS) for ocean altimetry applications [1]. A large variety of geophysical and geochemical parameters characterizing the reflecting surface can be measured by GNSS-R: over the years, the range of remote sensing tools enabled by GNSS-R has expanded enormously, finding applications in ocean remote sensing, atmospheric sounding, land/cryosphere mapping and hurricane forecasting (see review papers [2][3] for useful overviews on GNSS-R remote sensing). Nowadays, these techniques are entering a maturity phase, with satellite instruments currently orbiting such as the UK Tech-Demosat1 and the CYGNSS mission [4][5].

Another aspect of GNSS-based remote sensing relies on passive radar techniques. One of the most well established GNSS-based radar technologies is the passive Synthetic Aperture Radar (SAR) [6], which has been considered to map fixed objects on land and to monitor temporal land changes and deformations [7]-[10], while also exploiting spatial diversity to improve the quality of the output products [11]-[14]. Moreover, detection of moving targets has been addressed, [15], particularly for air targets such as airplanes and helicopters by considering forward-scattering radar modes [16]-[19].

An emerging application of the secondary use of GNSS signals is in the field of maritime surveillance. Some proof-of-concept investigations for ship target detection have been conducted considering GNSS-R, with specific reference to configurations comprising transmitter, airborne ([20])/spaceborne ([21],[22]) receiver and target aligned in the same direction. Coming to radar systems, first introductions to the concept of GNSS-based passive radar for maritime surveillance have been provided in [23][24]. The GNSS-based passive radar is particularly suited for the monitoring of maritime areas. As a passive system, it does not contribute to the electromagnetic pollution allowing the development of a light receiver that can be deployed in areas where active systems cannot be installed or are undesired for their harmful radiations (e.g., in marine protected areas) and it can benefit of the intrinsic covertness. The transmitted signals are a priori known (except few encrypted signals such as the GPS P-code reserved for military purposes), optimized for remote synchronization and they exhibit sufficiently wide bandwidths (e.g. over 10 MHz for Galileo E5 a/b or GPS L5) ; such standardization of GNSS sources assures that the same GNSS-based passive radar could be used in any part of the Earth without the need to customize it to match a specific local standard (i.e. waveform). A further strong benefit lies in the cost-effectiveness of the receiving hardware, which is very similar to commercial GPS receiver chipset used for navigation purposes. However, the main highlight of this technology lies in the design of the GNSS constellations, which provides a global coverage (even at the poles) and assures each point over the Earth' surface illuminated at any time by multiple satellites. In particular, 6–8 satellites simultaneously illuminate any point on Earth from different angles if a single GNSS constellation is considered; such number could rise up to 32 satellites with all the 4 global systems (GPS, GLONASS, Galileo and BeiDou) in full capacity. Noticeably, the global coverage ensured by navigation satellites makes them one of the few signal sources available in areas far from land such as economic exclusive zones and international waters. In such environments, passive radar activities based on terrestrial illuminators such as DVB-T, are prevented, while light receivers mounted on proper platforms such as moored buoys can exploit such reliable and ubiquitous sources representing a promising alternative. The main obstacle is represented by the restricted power budget provided by GNSS satellites. This prevents the applicability of this technology for wide area monitoring, and its

major use is mostly suited for short-range applications, such as supporting port operations, river navigation and maritime trade route control, or useful as a gap filler in areas where there is no persistent illumination.

In this framework, this paper focuses on the exploitation of the GNSS signals for ship targets imaging. This adds to current GNSS-based radar capabilities, namely the detection and localization of moving ships in the radar field of view, which have been the focus of previous research activities. Particularly, [23] and [24] refer to the exploitation of a single GNSS transmitter for detection purposes, while [25] and [26] make use of multiple transmitters to localize the target or to improve the detection performance with respect to the single transmitter case. The possibility to image the detected ships would represent an additional benefit, enabling target classification. Ship imagery may be obtained by resorting to Inverse SAR (ISAR) approaches. A few studies have addressed the imaging of ships via passive radar systems relying on illuminators other than GNSS. In particular, DVB-T based ISAR has been investigated in [27] while passive ISAR imaging systems based on geostationary telecommunication satellites or hitchhiking on a cooperative coastal radar have been proposed in [28]-[31] and [32], respectively.

As GNSS is not originally intended for radar purposes, it lacks the power budget and resolution capabilities of dedicated sensors, entailing a number of challenges for ISAR imaging. The fundamental bottleneck is represented by the very low power flux density near the Earth' surface. When the interest is mapping fixed objects on land, as in GNSS-based SAR, a suitable signal-to-noise ratio (SNR) can be obtained by considering long dwell times up to a few minutes [6]. In contrast, in the case of moving objects such as ships, increasing the SNR by considering extended dwells can be a demanding task. Two main factors make difficult extending the processing interval. First, the typical coherent processing interval (CPI) in this framework is in the order of 2-3 s [23], as ship de-correlation occurs for longer intervals. In addition, target motion prevents the possibility to accumulate the target energy over multiple CPIs if range and Doppler migrations are not properly handled. Therefore, in this paper we define an appropriate processing scheme able to effectively image the ships of interest. Specifically, as it will be detailed later on, in the case of ships providing a sufficiently high SNR in input to the receiver, such as vessels with large radar cross section (RCS) and/or at short receiver standoffs, the energy collected over a single CPI may suffice to isolate the target contributions from the disturbance background. In contrast, when the interest is in observing small and likely less reflective ships or ships at longer ranges, the separation of the target from the background requires longer dwells, even in the order of tens of seconds. E.g., in [24] it has been shown that an overall dwell over 30 s may be needed to detect a target with RCS 30 dBm2 at about 10 km from the receiver. In such circumstances, the ship image can be obtained by properly processing consecutive CPIs and suitably combing them non-coherently subsequently a procedure that compensates the energy migration in spite of the unknown ship dynamics [24].

It should be pointed out that, in order to achieve a useful representation of the target, it is required that the different scattering centers can be resolved and mapped into multiple resolution cells. In [33], a preliminary experimental investigation

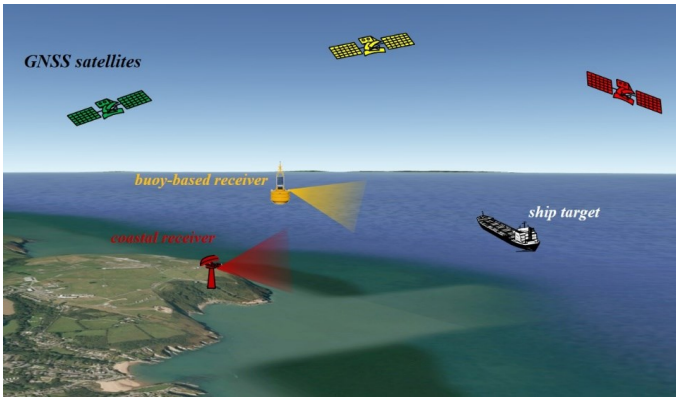

Figure 1. GNSS-based passive radar for maritime surveillance: system concept.

was carried out showing that, for ship targets of interest, the Doppler gradient observed by the receiver over proper CPIs can be larger than the related Doppler resolution, potentially enabling a cross-range profiling of the target. In addition, the range resolution provided by the GNSS signals with the largest bandwidths (up to 15 m for example for Galileo E5a/b) may provide the possibility of ship range profiling, albeit limited at vessels belonging to the highest dimensional classes (e.g., bulk carriers and large cruise ships). However, the natural domain where such radar images are produced is the bistatic range and Doppler plane (i.e., the basic plane) that is non-homogeneous and is changing with the considered transmitter. Indeed, for a comprehensive interpretation of the image products, the backscattered energy map has to be remapped into a homogeneous range – cross-range domain not changing with the considered transmitter. Particularly, this would enable the capability to extract from the imagery products relevant features characterizing the target, which can be sent to a classifier operator. In this regard, it is worth to notice that, due to the exploitation of waveforms of opportunity, we cannot expect images characterized by high resolution. Therefore, the main feature that could be extracted from the images is the geometrical information pertaining the target structure. To enable such capability, a suitable scaling technique is proposed able to remap the target energy into an equivalent monostatic range – cross-range plane thus allowing the length estimation (some preliminary results along this line have been presented in [34]). Although the GNSS-based passive images may not provide a fine classification capability due to the limited resolution properties, the estimation of the ship length can convey useful information about the detected target, providing an indication of the dimensional class to which the ship belongs. The conceived processing scheme has been tested against experimental data considering Galileo satellites and an opportunistic target undergoing different motion conditions. The achieved results prove the effectiveness of this technology at providing products from which key features of the ship could be extracted, thus nicely complementing the detection and localization stages.

The paper is organized as follows. Section II gives an overview of the GNSS-based passive radar for maritime surveillance. The ship target's imaging task is addressed in Section III, and the achieved results against experimental datasets are shown and discussed in Section IV. Section V closes the paper.

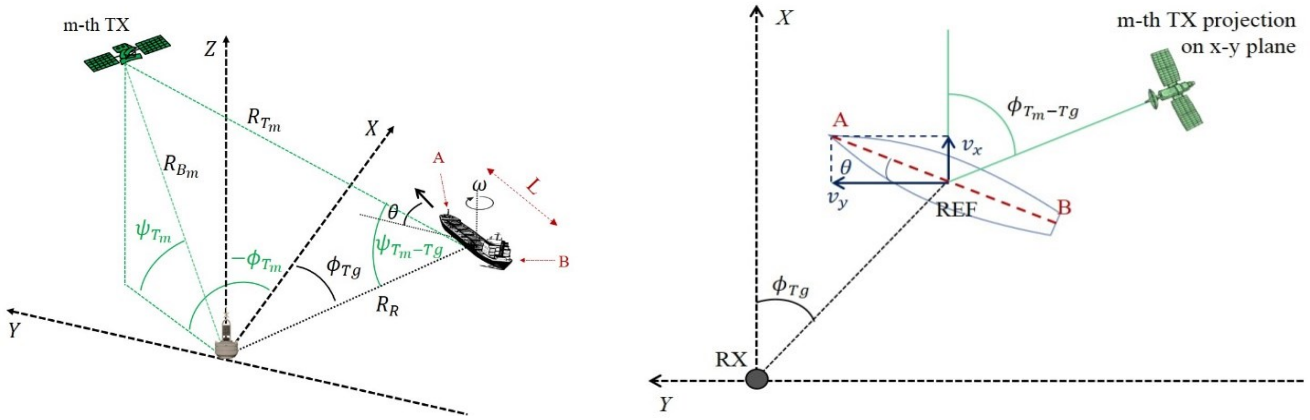

(a) (b)

Figure 2. (a) Overall system geometry: (b) Projection onto the (x, y) plane.

II. GNSS-BASED PASSIVE RADAR FOR MARITIME SURVEILLANCE

A general configuration of the GNSS-based radar system for maritime surveillance comprises navigation satellites, used as transmitters of opportunity, and a receiver that can be mounted on the coast or offshore on a buoy, as depicted in Figure 1. The parasitic receiver includes two channels: a reference channel that records the direct signal coming from the navigation satellites through a low-gain antenna and a surveillance channel that collects the weak reflected signal from the area under surveillance by means of a high-gain antenna. The targets to be detected, localized and imaged are vessels moving in the field of view of the surveillance antenna. In a general configuration, several satellites are considered and the receiver is able to separate the signals coming from the different satellites.

A. System geometry

The overall geometry is shown in Figure 2 (a): the assumed (O, x, y, z) Cartesian reference system has its origin coinciding with the receiver position (i.e. $\boldsymbol{Rx} = \{0, 0, 0\}^T$) and is obtained through as a rotation of the East-North-Up (ENU) reference system so that the x-axis coincides with the steering direction of the surveillance antenna. The trajectories of the transmitter and of the moving target during the observation time are described inside this local system.

Specifically, let M denote the number of visible satellites: the position of the m-th (m = 1, ..., M) transmitter is specified in the local plane by the vector $\boldsymbol{Tx_m}(t) = \{\mathrm{x_{Tm}}(t), \mathrm{y_{Tm}}(t), \mathrm{z_{Tm}}(t)\}^T$, being t the slow-time as defined in Section IIB, and by the angles $\phi_{\mathrm{Tm}}(t)$ and $\psi_{\mathrm{Tm}}(\mathrm{t})$ indicating azimuth and elevation, respectively. In particular, $\phi_{\mathrm{Tm}}(t)$ is the clockwise angle on (x, y) plane between x-axis and the satellite projection on (x, y) plane and $\psi_{\mathrm{Tm}}(\mathrm{t})$ is the out-of-plane angle between the (x, y) plane and the satellite. The target location is described by means of vector position $\boldsymbol{Tg}(t)$ and by the angle $\phi_{Tg}(t)$ that identifies the direction of arrival (DOA) measured clockwise from x-axis.

The instantaneous distance from the m-th transmitter to target, target to receiver and m-th transmitter to receiver are $R_{T_m}(t) = |\boldsymbol{Tx_m}(t) - \boldsymbol{Tg}(t)|$, $R_R(t) = |\boldsymbol{Rx} - \boldsymbol{Tg}(t)|$ and $R_{B_m}(t) = |\boldsymbol{Tx_m}(t) - \boldsymbol{Rx}|$, respectively. Therefore, the differential bistatic range is defined as

$$R_m(t) = R_{T_m}(t) + R_R(t) - R_{B_m}(t) \tag{1}$$

in which the compensation of the instantaneous baseline is taken into account [23], [24]. The bistatic Doppler frequency is equal to

$$f_m(t) = -\frac{1}{\lambda}\dot{R}_m(t) \tag{2}$$

where λ is the wavelength of the transmitted signal and the dot notation denotes the derivative with respect to t.

The generic motion of the vessel is decomposed as the superposition of the translation of a reference point (i.e., the vessel fulcrum) and of the rotation of the vessel around the fulcrum. The trajectory is thus identified by the time varying co-ordinates of the fulcrum: $\boldsymbol{Tg}(t) = \{\mathrm{x_{REF}}(t), \mathrm{y_{REF}}(t),\ 0\}^T$. The velocity vector, tangent to the trajectory and with variable direction during the acquisition, defines the heading angle $\theta(t) = tg^{-1}\left(\dot{x}_{REF}(t)/\dot{y}_{REF}\ (t)\right)$ measured clockwise from the y-axis. Changes in the direction of the velocity vector are taken into account by the angular velocity $(t) = \dot{\theta}(t)$, with a rotation axis normal to the ground plane. Therefore, a sketch of the target in the (x, y) plane is given in Figure 2 (b), where points A and B at distance L/2 from the fulcrum indicate the bow and the stern of the ship, where L is the ship length. Figure 2 also shows the angles ϕ_{T_m-Tg} [Figure 2 (b)], and ψ_{T_m-Tg} [Figure 2 (a)], that define the position of the m-th transmitter with respect to the target: in particular, omitting for the sake of simplicity the dependence on time, the angle $\phi_{T_m-Tg} = tg^{-1}\left\{\frac{y_{T_m}-R_R\cos\phi_{Tg}}{x_{T_m}-R_R\sin\phi_{Tg}}\right\} - \pi$ is measured in the (x, y) plane clockwise from the x-axis while the angle $\psi_{T_m-Tg} = tg^{-1}\left\{z_{T_m}/\sqrt{\left(x_{T_m} - R_R\sin\phi_{Tg}\right)^2 + \left(y_{T_m} - R_R\cos\phi_{Tg}\right)^2}\right\}$, defining the elevation of the satellite, is measured from the (x, y) plane.

B. Overall processing chain

In spite of the aforementioned benefits enabled by the choice of GNSS as opportunistic sources, their exploitation for radar purposes poses a number of technical challenges that have to be addressed. Figure 3 sketches the overall processing chain, from the reception of the direct and reflected signals up to the ship imagery. The stages devoted to the primary objectives of the system, namely the detection and localization of the ship targets, have been the focus of dedicated efforts in the past. As they are propaedeutic for the image formation task, they are here briefly described. The next section focuses on the dedicated signal processing stages to be implemented for the imaging and feature extraction procedures, representing the core of this work.

As GNSS signals are continuous wave, both the direct and reflected signals has to be preliminarily reformatted in an equivalent fast time & slow-time (τ, t) domain. This can be achieved by considering an equivalent pulse repetition interval (PRI) that can be selected as 1 ms, i.e., the typical duration of the transmitted pseudo random noise (PRN) code, so that $\tau \in [0, PRI]$ and $t \in [-T_a/2, +T_a/2]$, T_a being the overall observation interval. Moreover, the very low SNR in input to the receiver precludes the chance to use the direct signal as the reference for the matched filtering. A signal synchronization algorithm has to be performed, which essentially tracks the direct signals parameters (time delay, Doppler, phase and, if one exists, navigation message) and reconstructs a noise-free replica of the transmitted signal, thus enabling the range-compression of the surveillance channel data [6], [23].

Moving Target Indication (MTI) can be implemented by Doppler filtering. In most of passive radar system, this corresponds to reveal peaks in the bistatic Range-Doppler (RD) plane obtained over a short dwell, which in this application can be set equal to 2-3 sec [23]-[26]. Nevertheless, this conventional 'short-time' approach may fail in the system under consideration due to the limited transmitted power. Signal energy can be strengthen by considering longer dwells, as explained below.

The signal (in the range compressed & slow time domain) pertaining the overall integration time T_a is first segmented in N consecutive frames of short duration T_f (the CPI). Let $\dot{f}^*$ be an admissible value of the target Doppler rate and let us consider negligible range and Doppler migration at the single RD map level: the N frames feed the following steps, [23]:

Range migration compensation – According to the assumed motion model, the range migration experienced over the different frames is composed by a linear term (related to the target Doppler frequency) and by a quadratic term (related to the target Doppler rate $\dot{f}^*$). These can be compensated by multiplying each Doppler bin of the data in the fast-frequency and Doppler domain for a phase term comprising both the orders of migration.

Doppler migration compensation – Doppler migration from frame to frame is also related to $\dot{f}^*$: it can be compensated by multiplying the data in the range and slow-time domain for a proper phase ramp taking into account this source of migration.

Multi-frame integration – the RD maps pertaining the different processed frames and the same Doppler rate are incoherently integrated.

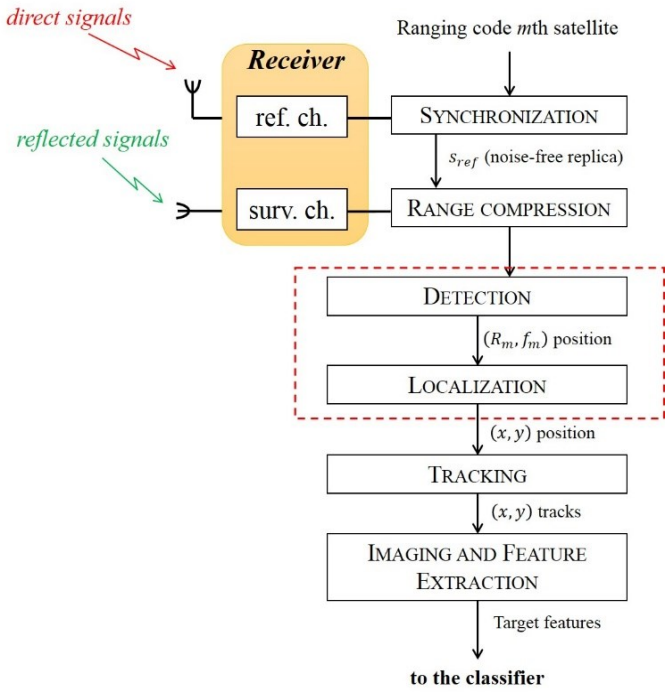

Figure 3. Overall processing chain.

A stack of integrated maps $RD(r, f, \dot{f})$ is therefore obtained with $\dot{f}$ varying in a properly defined interval bounded according to the maximum assumed velocity. Clearly, the maximum gain is obtained in the map pertaining the Doppler rate closest to the actual value. Then, a proper decision threshold is applied to each integrated map (for example by applying a 2D Cell Average Constant False Alarm Ratio, CA-CFAR, scheme) to detect the target. The integrated map of the stack over which detection occurs provides also an initial estimate of the target Doppler rate.

To move from the detected range and Doppler location to the target actual position, localization strategies have to be considered. It should be noted here that a single receiver could acquire signals transmitted from different satellites, essentially forming a passive multistatic radar system. As GNSS operate on code/frequency multiple access schemes, a single receiver can perform MTI operations on multiple bistatic geometries and therefore multi-lateration approaches can be considered to retrieve the target location [25]. A different strategy to exploit the inherent multistatic nature of the GNSS-based passive radar consists in merging the detection and localization procedures (red dotted box in Figure 3) resorting to a single-stage approach to localize the target while improving its probability of detection, [26].

Subsequently, the estimated target locations achieved over consecutive integration windows can be sent to a tracker stage to retrieve the targets' trajectories, so that the estimated kinematic parameters of the target, i.e. $\widehat{\boldsymbol{Tg}}(t)$ and $\hat{\theta}(t)$, can be made available to the successive stage. This stage can implement conventional approaches based on Kalman filtering, particle filter [35] or probability hypothesis density [36]. Additionally, it is worth to mention that detection and tracking stages could be combined by resorting to track-before-detect methods to increase the capability of the system to detect the

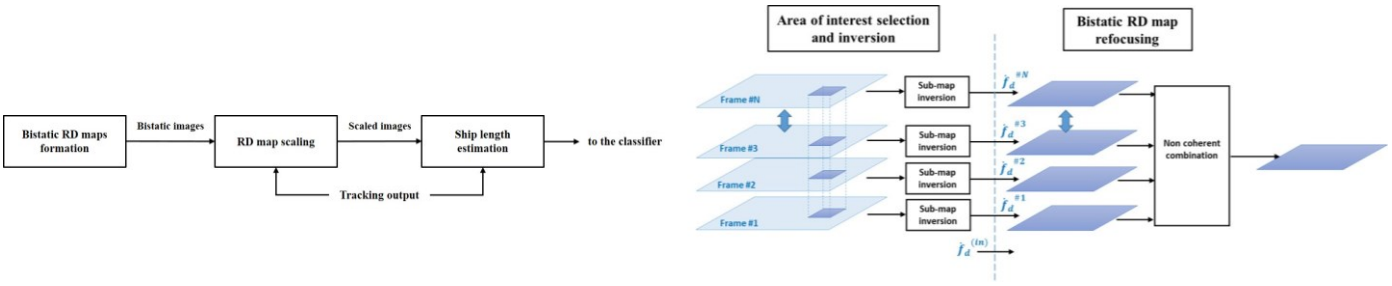

(a) (b)

Figure 4. (a) Imaging and feature extraction processing scheme; (b) Target RD map refocusing processing scheme.

targets in this frame of low power budget. Some investigations toward this direction can be found in [37].

The final stage consists of the formation of radar images of the target from which retrieving relevant features, so providing advanced capability to the GNSS-based passive radar. The conceived technique for this purpose is described in the following section.

III. PASSIVE RADAR IMAGERY OF SHIP TARGETS

As mentioned above, once the target has been detected and localized, the imaging/feature extraction stage can be applied. The possibility to image the target and extract some features arises when the target energy spans over multiple range and/or Doppler resolution cells and when the signal is reflected by several scattering centers.

A flow chart that pictures the processing proposed for imaging is shown in Figure 4 (a): the processing comprises two main steps, namely target RD map focusing and range/cross-range scaling. The considered chain receives the stack of RD maps corresponding to the integrated map $RD\left(r,f,\dot{f}^{(Tg)}\right)$ over which the target has been detected and then provides in output the scaled images/profiles.

Target focusing is based on [Figure 4 (b)]:

Area of interest selection and inversion mapping stage – In order to image the detected target, it is necessary to separate the target signal components from the received signal containing also noise, clutter (and possibly other targets). This is an important step of the image formation process. In fact, in the case of multiple targets in the surveyed area, each must be separately processed by the imagery processor. Moreover, discarding most of the range and Doppler bins outside the area of interest sensibly alleviates the computational burden required by the following stages. Finally, as it will be detailed later, the RD map refocusing stage relies on an image contrast optimization procedure, which will benefit of an evaluation on a sub-map mainly occupied by the target returns since this cropping improves signal to background conditions by discarding background contributions outside the window.

The selection of the area of interest is implemented directly on the stack provided in input by exploring spatial concentration. It is a windowing process that crops a rectangular area from the RD maps around the target position with proper bounds set according to the maximum possible ship extent. The resulting sub-maps are then back-mapped into the slow time domain by applying the inverse Fourier transform. These back-mapped sub-maps, $s_{TMC}^{n}(r,u)$ with $u \in \left[-T_f/2,\ T_f/2\right]$, together with the initial estimated of the target Doppler rate, i.e. $\dot{f}_d^{(in)} = \dot{f}_d^{(Tg)}$, are provided in input to the successive stage.

Target RD map refocusing and scaling stage – This is based on the following assumptions:

1. The migration compensation, both in range and in Doppler, applied at the detection stage according to the $\dot{f}_d^{(in)}$ value basically compensates the migration caused by the translation motion;
2. Oscillations/rotation motions can cause an additional source of Doppler migration that may need additional compensation at the frame level. Only Doppler is considered due to the coarse range resolution.
3. As the detection stage, also the image formation comprises a coherent and a non-coherent processing. Particularly the N image products achieved over consecutive CPIs are non-coherently combined to form a multi-frame target image.

In particular, to cope with point 2, an additional Doppler migration compensation is included. As the final image products are likely characterized by coarse resolutions, inside each frame a second order phase behavior can be assumed [38]; therefore, , the in frame migration is compensated via a proper dechirping. Furthermore, to cope with time variant characteristics, the Doppler rate value driving the in frame dechirping is allowed to vary from frame to frame (i.e., N different values are involved). Therefore, the target image is obtained via autofocus by compensating the in frame Doppler migrations according to the N-tuple that maximizes the contrast of the final image, i.e.

$$\left(\dot{f}_d^{\#1}, \dot{f}_d^{\#2}, \dots, \dot{f}_d^{\#N}\right)_{opt} = \arg\left\{\max_{\dot{f}_d^{\#1}, \dot{f}_d^{\#2}, \dots, \dot{f}_d^{\#N}} \left[IC\left(RD_{Tg}\left(r, f_d, \dot{f}_d^{\#1}, \dot{f}_d^{\#2}, \dots, \dot{f}_d^{\#N}\right)\right)\right]\right\} \quad (3)$$

$$RD_{Tg}\left(r, f_d, \dot{f}_d^{\#1}, \dot{f}_d^{\#2}, \dots, \dot{f}_d^{\#N}\right) = \frac{1}{N}\sum_{n=1}^{N}\left|\mathfrak{F}_u\left\{s_{TMC}^{n}(r,u)e^{-j\pi\dot{f}_d^{\#n}u^2}\right\}\right|^2 \quad (4)$$

$IC(*)$ being the contrast, defined as the ratio of the standard deviation of the image to its mean value, and $\mathfrak{F}_u\{*\}$ is the Fourier transform over slow time u.

Concerning point 3, it is likely that during the long observation time involved, different target scatterers can be

visible to the radar: the hybrid combination will combine them all with the specific aim to reconstruct the target segment so that features like the target dimensional class could be estimated.

It is worth to point out that in the procedure above the target image/profile is obtained by exploiting the same time intervals adopted at the detection stage. Particularly, the coherent imaging interval have been selected equal to T_f and N frames have been considered to produce a multi-frame image via the non-coherent summation in (4). This allows the processing chain to operate directly on the motion compensated RD maps available from the detection stage. However, the procedure could be easily generalized to cope with imaging intervals others than those exploited to detect the target.

A further comment concerning the possibility of the proposed processing chain to provide real-time ship monitoring is in order. In the processing stages detailed in Section II, the main bottleneck of the computational load hindering real-time operations is represented by the detection stage, as it requires to implement multiple range and Doppler migration compensations for different admissible values of the target Doppler rate. Nevertheless, as the same operations must be implemented for each tested Doppler rate, the detection processing is highly parallelizable. By exploiting specialized tools for parallel processing such as Graphic Processing Units (GPU), the execution time can be drastically reduced. In our test, by properly adapting the motion compensation procedure for implementation on GPU and considering non-coherent integration intervals of 30 s, we were able to achieve rate of update of the detection output less than 3 s, which is compliant with the usual requirements for maritime surveillance applications. Moreover, the detection process could be further speed up by properly combining the motion compensation procedure with track-before-detect methods (see [37]). About the Imaging and Feature Extraction stage, the key element to save the execution time is the windowing operation accomplished during the area of interest selection, greatly reducing the amount of data to be processed during the target RD map refocusing. Moreover, the searching procedure (3), (4) can benefit of the availability of the starting points of the search (i.e., $\dot{f}_d^{(in)}$). Therefore, even though the optimization of the whole procedure to achieve real-time ship imagery is a separate topic worthy of its own investigation, the considerations outlined above suggest that real-time passive ship imagery with this technology is fundamentally possible.

Obviously, the ship images achievable from the processing above are strictly dependent on the motion of the target: in particular, when the target exhibits a pure radial motion, a range profile is obtained (i.e., no Doppler separation), whereas when the motion is almost tangential a Doppler/cross-range profile is obtained (due to the coarse range resolution, no range separation among the different target scatterers) and, finally, when both components are not negligible a complete image could be obtained (separation in both range and Doppler dimensions, depending also on the size of the target). Usually, ISAR images are scaled in the monostatic range & cross-range domain in order to extract the target features. Starting from the bistatic range & bistatic Doppler map, the bistatic range can be converted into monostatic target-to-receiver range and the bistatic Doppler can be changed into cross-range axis by means of range and cross-range scaling factors, respectively. Such factors, needed for the scaling, are separately derived in the two following sub-sections.

A. Range scaling

Starting from (1), we can write the target bistatic range as follows:

$$R_m(t) = R_R(t) + R_{(T-B)_m}(t) \tag{5}$$

where $R_{(T-B)_m}(t) = R_{T_m}(t) - R_{B_m}(t)$ is the component of the bistatic range dependent on the transmitter.

Taking into account that $R_{T_m}, R_{b_m} \gg R_R$, (5) can be approximated by replacing $R_{(T-B)_m}$ with its first order Taylor Series approximation centered around the receiver position:

$$\begin{aligned} R_{(T-B)_m} &\approx -\frac{x_t \cdot x_{Tm} + y_t \cdot y_{Tm}}{\sqrt{x_{Tm}^2 + y_{Tm}^2 + z_{Tm}^2}} = \\ &= -R_R \cdot \left[\cos(\psi_{Tm}) \cos\left(\phi_{Tm} - \phi_{Tg}\right)\right] \end{aligned} \tag{6}$$

(x_t, y_t) being the coordinates of a generic point of the target and where the dependence on slow-time has been omitted for brevity. Hence, R_m is approximated as

$$R_m \approx R_R \cdot k_{r_m} \tag{7}$$

where k_{r_m} is the range scaling factor given by

$$k_{r_m} = 1 - \cos\left(\psi_{T_m}\right) \cos\left(\phi_{T_m} - \phi_{Tg}\right) \tag{8}$$

The bistatic range R_m is thus scaled and mapped into an equivalent monostatic target to receiver range R_R according to the value of the scaling factor k_{r_m} at the specific image time. Consequently, the monostatic range resolution is achieved as

$$\rho_{r_m} = \frac{\rho_R}{k_{r_m}} \tag{9}$$

In the equation above, ρ_R equals to $\alpha_r \, {}^{c}/_{B}$, α_r being the factor accounting the shape of the autocorrelation function of the transmitted signal (well approximated as a triangular function [7], [11]).

As evident from (8), the scaling factor depends on the target direction of arrival ϕ_{Tg}: the motion parameters retrieved in the localization/tracking stage can be exploited for the evaluation of the scaling factor.

B. Cross-range scaling

In order to derive the cross-range scaling factor, we first derive the target instantaneous Doppler bandwidth defined as the range of Doppler frequencies span from point A to point B, see Figure 2 (a), namely

$$B_{d_m} = \left| f_{d_m}^{A} - f_{d_m}^{B} \right| \tag{10}$$

where $f_{d_m}^{A}$ and $f_{d_m}^{B}$ are the Doppler frequency of the points A and B, respectively, at the image time. It is worth to underline that here the term "cross-range" is used in a wide sense referring to the direction given by the line through points A and B.

From the mathematical model described in Figure 2, the instantaneous Doppler bandwidth consists of four contributions as follows

$$B_{d_m} = \left| B^R_{d\,\omega} + B^{T_m}_{d_\omega} + B^R_{d_V} + B^{T_m}_{d_V} \right| \tag{11}$$

where $B^R_{d\,\omega}$ and $B^{T_m}_{d_\omega}$ are the Doppler bandwidth contributions due to the target rotation with respect to the receiver and the m-th transmitter, respectively, while $B^R_{d\,V}$ and $B^{T_m}_{d_V}$ are the Doppler bandwidth contributions due to the target translation with respect to the receiver and the m-th transmitter, respectively.

The component $B^R_{d\,\omega}$ can be written as, [40]

$$B^R_{d\,\omega} \cong -\frac{1}{\lambda}\overline{AB}\cos\left(\theta - \phi_{Tg}\right)\omega \tag{12}$$

where $\omega = \dot{\theta}$ is the angular velocity calculated at the image time and $\overline{AB}\cos\left(\theta - \phi_{Tg}\right)$ is the projection of $\overline{AB}$ on the normal to the line joining the receiver and the target reference point (i.e., the receiver Line-Of-Sight LOS).

The contribution $B^{T_m}_{d_\omega}$ can be calculated as

$$B^{T_m}_{d_\omega} \cong -\frac{1}{\lambda}\overline{AB}\cos\left(\theta - \phi_{T_m - Tg}\right)\cos\left(\psi_{T_m}\right)\omega \tag{13}$$

where $\overline{AB}\cos\left(\theta - \phi_{T_m - Tg}\right)$ is the projection of $\overline{AB}$ on the normal to the line joining the m-th transmitter and the target reference point and $\cos(\theta_T)\,\omega$ represents the effective rotation rate with respect to the transmitter LOS.

Regarding the translational motion, it is worth to underline that only the component referred to the receiver contributes to the formation of the Doppler bandwidth. In fact, due to the large distance between the target and the transmitter, the contribution $B^{T_m}_{d_V}$ can be neglected as it should be much smaller than the Doppler resolution cell ($1 / T_f$).

In order to evaluate $B^R_{d_V}$, we start by writing the Doppler frequency of the generic point of the target with coordinates (x_t, y_t) at distance R_R

$$f_d(x_t, y_t) = -\frac{V_r(x_t, y_t)}{\lambda} = -\frac{V}{\lambda}\sin\left(\theta + \phi_{Tg}\right) \tag{14}$$

where $V_r(x_t, y_t)$ is the radial component of the velocity for the target point under consideration and V denotes the absolute value of the velocity: the bandwidth of interest can thus be obtained as the product of the directional derivative of the Doppler frequency along the direction connecting points A and B evaluated at the target fulcrum by the length between point A-B, namely (15) shown bottom to this page, where $\nabla f_d = \left[\frac{\partial f_d}{\partial x_t}, \frac{\partial f_d}{\partial y_t}\right]^T$ and $\hat{u} = [\sin\theta\,, \cos\theta]^T$ is the unit vector associated to the $\overline{AB}$ line.

Finally, (11) can be rewritten as (16) shown bottom to this page. Therefore, the cross-range scaling factor is obtained as (17) shown bottom to this page.

Therefore, the cross-range resolution is given by

$$\rho_{cr_m} = \frac{1}{T_f\, k_{cr_m}} \tag{18}$$

As already observed for the range scaling, the evaluation of the cross-range scaling factor also requires the knowledge of target-related parameters: as above, the relevant information can be easily retrieved from the output of the localization/tracking stage. Obviously, errors in the knowledge of these relevant target kinematic parameters can have an impact on the scaling steps (and, as a consequence, this can result in an error in the extracted target length). While a complete characterization of the accuracy provided by the localization and tracking stage would be beyond the scope of this manuscript, the reader is referred to Section IV.B for a simplified theoretical analysis to get some insight the sensitivity of the scaling stage.

C. Ship length estimation

The estimation of the target features can be performed in the range domain or in the Doppler domain depending on the target's motion. Particularly, the radial and tangential components of the motion can be evaluated by measuring the rate of changes of the target range and Doppler histories. If the target motion is predominantly radial, the target length can be estimated from the number of range cells over which target energy spans, as in this case it is $B_d < 1/T_f$. As described above, the bistatic range has to be first converted into the monostatic range, so that it is then possible to estimate directly the slant range ship length, $\hat{L}_{slant}$, as the size of the ship segment in the range direction: the physical target length can be derived projecting $\hat{L}_{slant}$ on the heading direction through the relationship

$$\hat{L} = \hat{L}_{slant}/cos(\theta) \tag{19}$$

In contrast, in the case of dominant tangential motion, the information related to the target size can be retrieved from the estimated Doppler bandwidth of the ship segment. Indeed, in this case $B_d >> 1/T_f$. The Doppler bandwidth can be measured

---

$$B^R_{dV} \cong \left(\nabla f_{d\,|(x_{REF}, y_{REF})} \cdot \hat{u}\right)\overline{AB} = \frac{V}{\lambda R_R} cos\left(\theta + \phi_{Tg}\right)\left(sin\,\phi_{Tg}\,sin\,\theta - cos\,\phi_{Tg}\,cos\,\theta\right)\overline{AB} = \\ = -\frac{V}{\lambda R_R} cos^2\left(\theta + \phi_{Tg}\right)\overline{AB} \tag{15}$$

$$B_{d_m} \cong \frac{1}{\lambda}\left|\left(\cos\left(\theta - \phi_{Tg}\right) + \cos\left(\theta - \phi_{T_m - Tg}\right)\cos\left(\psi_{T_m}\right)\right)\omega + \frac{V}{R_R} cos^2\left(\theta + \phi_{Tg}\right)\right| \overline{AB} \tag{16}$$

$$k_{cr_m} = \frac{1}{\lambda}\left|\left(\cos\left(\theta - \phi_{Tg}\right) + \cos\left(\theta - \phi_{T_m - Tg}\right)\cos\left(\psi_{T_m}\right)\right)\omega + \frac{V}{R_R} cos^2\left(\theta + \phi_{Tg}\right)\right| \tag{17}$$

on the range-Doppler map and the target length can be calculated through the relationship

$$\hat{L} = \hat{B}_{d_m} / k_{cr_m} \tag{20}$$

Otherwise, passing in the cross-range domain through the cross-range scaling (16), the length can be measured directly on the scaled map.

In the case of mixed motion with jointly relevant radial and tangential components, both the range and Doppler information could be exploited for the length estimation task. In such cases, the estimation can be performed exploiting the domain providing the best resolution over the ship axis direction. In the case of range scaling, the ship length resolution is obtained as the monostatic range resolution (9) scaled by the cosine of the heading direction. Whereas in the cross-range domain, as the proposed cross-range scaling directly projects the Doppler axis over such direction, the ship length resolution coincides with ρ_{cr_m}.

Whether the ship length is estimated exploiting the range or the Doppler information, the target edges must be extracted from the images to perform a reliable measurement of $\hat{L}_{slant}$ and $\hat{B}_d$ (or $\hat{L}$), which is usually in the scope of segmentation procedures. The study and development of advanced segmentation procedures specifically tailored for the system under consideration is a subject for further study. However, a preliminary approach to extract the target edges has been here considered as follows.

Let ι_n be a pixel of the nth frame complex image, a binary hypothesis test can be written as

$$\begin{aligned} \mathcal{H}_0&: \ \iota_n = w_n \\ \mathcal{H}_1&: \ \iota_n = A_n + w_n \end{aligned} \tag{21}$$

Under the null hypothesis $\mathcal{H}_0$, the pixel contains disturbance background only, here modeled as white Gaussian characterized by power σ_w^2, i.e., $w_n \sim \mathcal{CN}(0, \sigma_w^2)$ where $\mathcal{CN}$ denotes the complex normal distribution. Under the alternative hypothesis $\mathcal{H}_1$, ι_n contains both disturbance and return of a scatterer of the target, the latter having complex amplitude A_n that can be modeled as a zero-mean complex normal random variable with variance σ_a^2, i.e., $A_n \sim \mathcal{CN}(0, \sigma_a^2)$. This model takes into account that (i) the system is noise limited rather than clutter limited [24] and (ii) scatterer reflectivity may vary over the different frames.

To isolate the target edges from the background, a decision threshold η is selected according to a desired level of false alarm rate P_{fa} to decide if each ι_n belongs to $\mathcal{H}_0$ or $\mathcal{H}_1$. Taking into account the image formation procedure (4), which basically performs a non-coherent quadratic integration over N frames, it could be shown that the relationship between P_{fa} and η is given by

$$P_{fa} = 1 - \frac{\gamma\left(N, {}^{\eta}/_{\sigma_w^2}\right)}{\Gamma(N)} \tag{22}$$

where $\Gamma(\cdot)$ is the Gamma function and $\gamma = \int_0^b t^{a-1} e^{-t} dt$ is the lower incomplete Gamma function. The noise power can be estimated by exploiting a region of the RD plane containing no target returns.

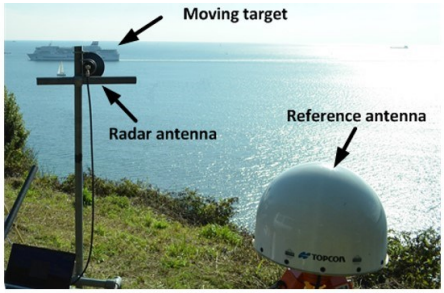

(a)

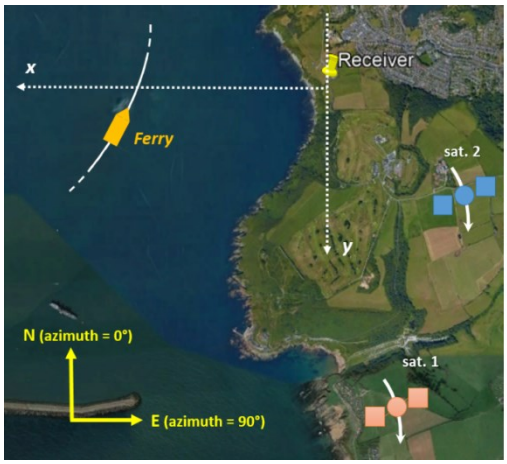

(b)

(c)

Figure 5. Experimental campaign: a) experimental receiver, b) acquisition geometry, c) non-cooperative target 'Brittany ferry'.

By thresholding according to (22), a binary image can be obtained allowing extracting the target area from the disturbance background. Standard morphological operators such as region-growing and region filling can be also considered to cluster the remaining image regions [41]. Large regions close to the main body of the target are retained, while isolated peaks out of the main body are discarded. Then, the extent of the ship along the range/cross-range direction can be evaluated as the maximum distance between the revealed segments.

Finally, it should be noted that (22) gives also a direct measure of the improvement factor deriving from the multi-frame image formation approach. Even though the combination of multiple frames cannot increase the range and cross-range resolutions, it allows not only to strengthen the target contribution but also to use a lower threshold than the single frame case while maintaining the same level of false alarms. Consequently, lower intensity pixels belonging to the target will have more chances to be extracted in the multi-frame image.

Table I Experimental and signal processing parameters

Parameter		Unit	Value
Satellite 1	Number	-	GSAT0201
	Ranging code	-	PRN E18
	Azimuth angle	degree	163.8 ~ 163.9
	Elevation angle	degree	18.9 ~ 18.2
Satellite 2	Number	-	GSAT0203
	Ranging code	-	PRN E26
	Azimuth angle	degree	158.1 ~ 158.4
	Elevation angle	degree	49.6 ~ 48.7
Carrier frequency		MHz	1176.45
Chip-rate (signal bandwidth)		MHz	10.23
Sampling frequency		MHz	50
Dwell time		s	145
Equivalent pulse repetition interval		ms	1
Frame duration (CPI)		s	3
Non-coherent processing interval		s	15
Surveillance antenna gain		dBi	16
Surveillance antenna polarisation		-	Left-hand circular
Surveillance antenna 3 dB beamwidths		degree	30 (azimuth), 30 (elevation)
Receiver noise figure		dB	1.5

IV. EXPERIMENTAL RESULTS

The effectiveness of the proposed method has been demonstrated by using data acquired in an experimental campaign carried out at the Plymouth Harbor, UK. The experimental campaign is detailed in Figure 5. The experimental hardware comprises a super-heterodyne receiver developed at the University of Birmingham, UK, equipped with a reference and a surveillance channel [Figure 5 (a)]. During the trials, the receiver was placed on the shore, acquiring direct and reflected signals emitted by Galileo satellites [Figure 5 (b)]: particularly, for the following analysis, the E5a-Q signal is considered. The target of opportunity was a commercial Brittany ferry, whose optical photograph is shown in Figure 5 (c). This vessel has length 184 m and beam 25 m. Its Automatic Identification System (AIS) message was also recorded in real-time during the experiment for comparison with the experimental results. Two satellites in view of the receiver were successfully synchronized and exploited in the processing chain depicted in Figure 3. The experimental and signal processing parameters are listed in Table I. The results concerning the detection and localization of the target are briefly shown in sub-section A, while sub-section B is devoted to the imaging results.

A. Target detection and localization

Figure 6 shows the RD maps obtained exploiting the individual baselines. A CPI equal to 3 s was selected [23], and by means of Doppler filtering (i.e., FFT) the single-frame maps in Figure 6 (a) and (b) were obtained for sat. 1 and sat. 2, respectively. Moreover, by applying target motion compensation and non-coherent integration of N = 5 frames (namely, overall integration windows last 15 sec), the long-time RD maps in Figure 6 (c) and (d) were obtained. In all the maps, 0 dB denotes

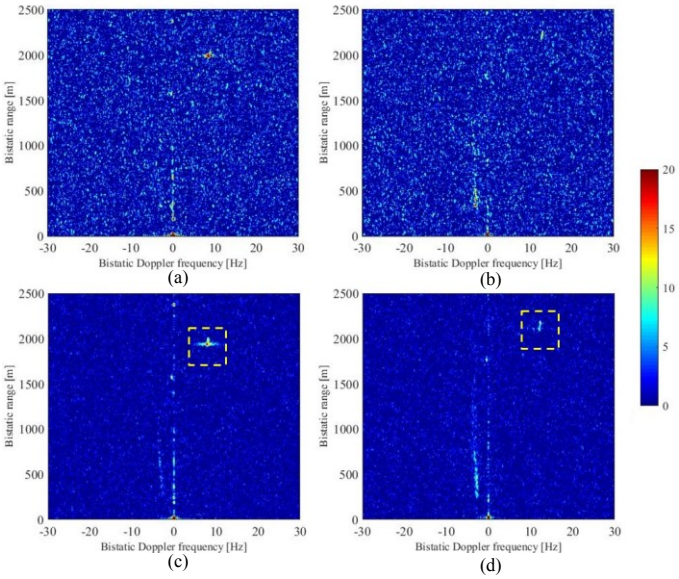

Figure 6. Experimental RD maps – a) sat. 1, single frame, b) sat. 2, single-frame c) sat. 1, multi-frame, d) sat. 2, multi-frame.

the mean background power. The strong return located at the zero range and zero Doppler position is the compressed direct signal (along with its sidelobes) received in the surveillance antenna. These could be filtered out, as the stationary background, but here we retained it for sake of comparison with the amplitude levels of background and target. Moreover, looking at the long-time maps is it possible to observe bright points (highlighted by the yellow boxes) for both satellites corresponding to the actual target position. Thanks to the reduction of the background fluctuations because of the multi-frame combination [well visible by comparing Figure 6 (a) and (b) with Figure 6 (c) and (d)], the target can be easily detected in both the maps. It is worth to notice that the ship echoes are quite visible even in the corresponding single-frame maps. Indeed, as a proof-of-concept study, a target with a relatively high size/RCS was deliberately sought. Consequently, in these particular conditions a very long integration time is not strictly required to make it detectable. Nevertheless, when illuminated by sat. 2, the target return is weaker, with a peak power around 10 dB lower than sat. 1. (This behavior could be due to the lower elevation angle of sat. 1, making this geometry closer to a backscattering configuration, which is supposed to be more suited for GNSS-based maritime surveillance, [20], [22].). Due to the different bistatic angles involved in the system, strong variations of the reflected energy are easily observed, so that even large targets could results in low SNR values in particular satellite viewing angles [26]. Although in this specific case the target could be detected even by applying straightforward Doppler filtering, the long integration time technique can enhance the quality of the detection and localization results even for this massive target [23],[24],[26]. Likewise, it will be shown in the remainder of the paper that this can improve the quality of the image product as well.

By applying the procedure over consecutive integration windows by shifting the starting time of 1 second, 131 long-time RD maps have been obtained for each baseline. A thresholding and clustering stage can be subsequently applied to each map thus obtaining the instantaneous range and Doppler position of

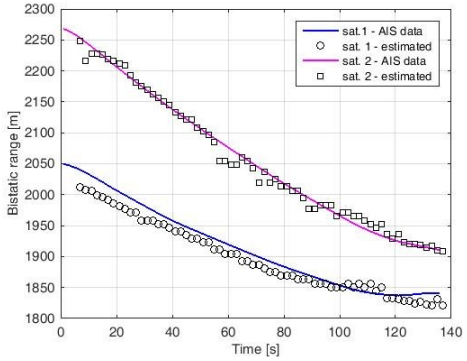

(a)

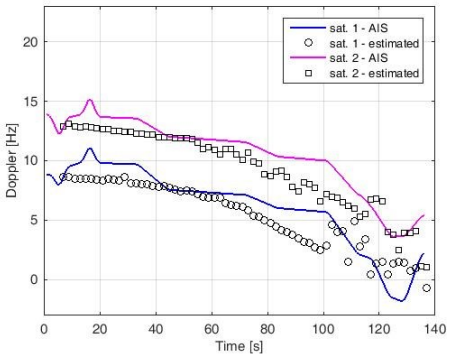

(b)

Figure 7. AIS vs estimated bistatic range (a) and Doppler (b) positions.

the target in the different bistatic planes. Figure 7 shows the estimated range and Doppler histories compared with the AIS ground truth, highlighting a good correspondence between estimated and actual target positions. Then, based on the measured range positions as seen by the two satellites, the ferry has been localized during its path via multi-lateration [25]. The obtained Cartesian track is shown in Figure 8, with a good degree of coincidence with the AIS ground truth.

B. Imaging results

By inspecting the detected range and Doppler history, it could be shown that at the beginning of the acquisition, the target is approaching with a predominantly radial motion. Therefore, by selecting RD maps within this interval, relevant information concerning the target size can be obtained over the range domain. Figure 9 shows the images obtained at the same image time by considering the two satellites viewing angles, where the 0 dB level denotes the mean background power. Such images, centered in the target fulcrum, have been obtained by using an individual CPI as image interval (namely, these are single frame images). Following the procedure described in Figure 4, after cropping the patch of the RD maps containing the target, radar images have been obtained by searching the value of the Doppler rate maximizing the intensity contrast. The resulting IC values as a function of the tested Doppler rates are shown in Figure 10. It is possible to observe that for both the perspectives the maximum value is reached for the null Doppler rate. This is well in line with the theoretical expectations and, therefore, in these particular conditions the refocusing step could be skipped here. For the same reason, in this case the images are in the monostatic range and bistatic Doppler domain. Indeed, the cross-range scaling has not been applied here: due to the small

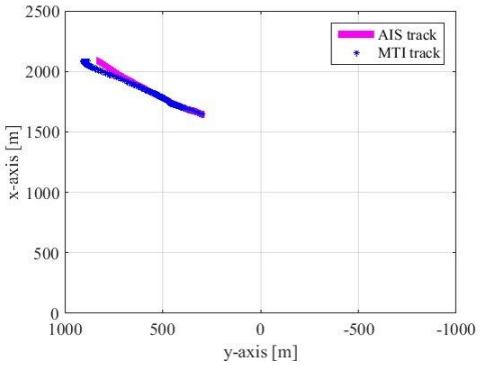

Figure 8. Target Cartesian track.

tangential component of the target velocity, the Doppler gradient is smaller than the Doppler resolution cell, preventing a meaningful cross-range profiling. Nevertheless, from the images a significant spread of the energy along the range direction can be easily observed, giving rise to the possibility to extract useful information pertaining the target size.

To accomplish the range-scaling (8), two different operative conditions have been considered. In the former, the target direction of arrival has been calculated from the estimated track (i.e., the MTI, track) [Figure 9 (a) and (c)], while in the latter we used the information obtained from the AIS [Figure 9 (b) and (d)]. The images obtained starting from the MTI or the AIS data are very similar, proving the effectiveness of the procedure proposed to image the target by extracting its kinematic parameters directly from the received data. By measuring the spread of the energy over the range direction (further details on how to perform this task will be discussed later on) and by projection over the target heading direction (using the MTI/AIS data in (17)), the ship length is estimated equal to 144 m (using AIS information) and 132 m (using the MTI information) for sat. 1, and equal to 148 m (AIS) and 135 m (MTI) for sat. 2. It is also worth to observe the different level of SNR resulting in the images pertaining the different bistatic channels. As already pointed out, the ferry backscattered a lower amount of energy when illuminated by the second satellite and therefore, for a comprehensive representation of the images, different colorscales have been used to show images pertaining sat. 1 and sat. 2.

During the acquisition, the target maneuvered so that its trajectory became nearly tangential to the surveillance antenna steering direction. Figure 11 shows single-frame images obtained at image times within this period in the monostatic range and cross-range domain. As for Figure 9, also in this case the images have been centered in the target fulcrum and 0 dB denotes the mean background power level. In such a case, it has been necessary to re-focus the images to obtain higher quality products: indeed, as expected, not null values of the Doppler rate provide the highest intensity contrasts, as shown in Figure 12. In these particular motion conditions, the resulting images are appropriate to perform cross-range profiling and in fact, a visible spread of the target energy along the cross-range direction can be observed.

As for the previous case study, the scaling has been performed exploiting both the AIS [Figure 11 (a) and (c)] and the MTI

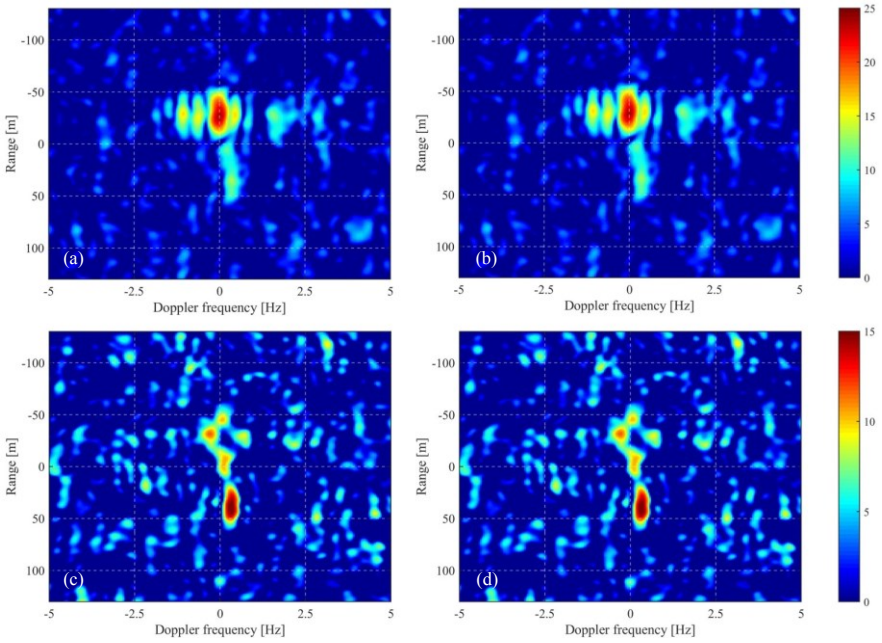

Figure 9. Dominant radial motion – Single frame monostatic range & bistatic Doppler maps obtained for (a) sat. 1 with AIS (b) sat. 1 with MTI (c) sat. 2 with AIS (d) sat. 2 with MTI.

information [Figure 11(b) and (d)]. Using these images, the target length has been evaluated as L = 173 m (AIS) and L = 169 m (MTI) for sat. 1 and L = 136 m (AIS) and L = 142 m (MTI) for sat. 2, respectively. As for the radial case, also for the case of a target undergoing maneuvers, we observe a good correspondence between images scaled with the AIS and MTI data and extracted lengths. Such correspondence between products each obtained by exploiting information sources (MTI and AIS) interested by different errors implicitly validates the proposed scaling procedure and demonstrates its robustness. To further analyze the impact of inaccuracies in the relevant target kinematic parameters (target range, direction of arrival, direction of motion, speed and rotation rate) on the scaling stage, we evaluate the performance degradation arising under the hypothesis of random errors in the knowledge of the needed parameters. Particularly, the degradation of the scaling performance is evaluated in terms of the mean value and the standard deviation of the scale factor estimation error normalized w.r.t. the scale factor achieved in the ideal condition (i.e., ideal knowledge of the kinematic of the target) for both cases of dominant radial motion and maneuvering target. In particular we consider the parameter value used inside (8) or (17) equal to $\hat{\gamma} = \gamma_0 + \varepsilon_\gamma$ being γ_0 the true value of the parameter, ε_γ a zero mean Gaussian random variable with standard deviation equal to $\eta_\gamma \gamma_0$ and γ equal to the target range (R_R), direction of arrival (ϕ_{Tg}), direction of motion (θ), speed (V) and rotation rate (ω). In this analysis transmitters/receiver locations have been set according to the experimental configuration, the true values of the target motion parameters have been set equal to the AIS values and the random errors have been considered to interest all the parameters under the simplifying assumption of uncorrelated errors. Even if such procedure is approximated, it can give us a reasonable idea of the robustness of the proposed technique.

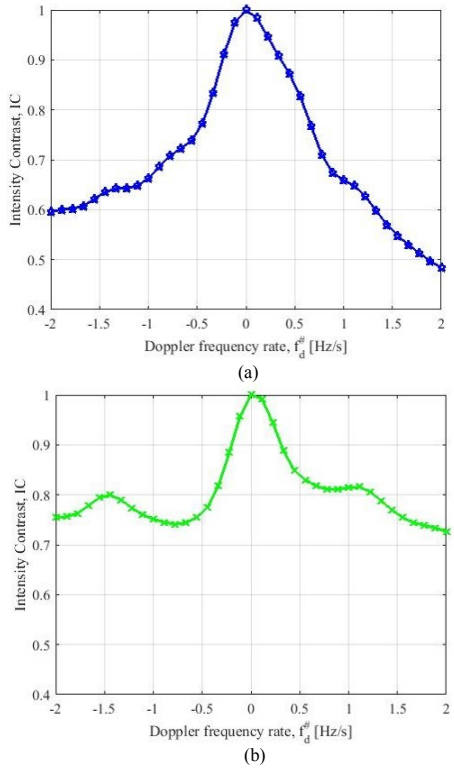

Figure 10. Intensity contrast as a function of the Doppler rate for sat.1 (a) and sat. 2 (b) in the case of a dominant radial motion.

Starting from the dominant radial motion case (the one corresponding to results in Figure 9), Table II shows the mean value and standard deviation of the normalized scaling factor error as obtained by averaging over 10^5 independent realizations of $\widehat{\phi_{Tg}}$. Results of a similar analysis for the dominant cross-range motion case (the one corresponding to results in Figure 11) are reported in Table III. Particularly, in this second case,

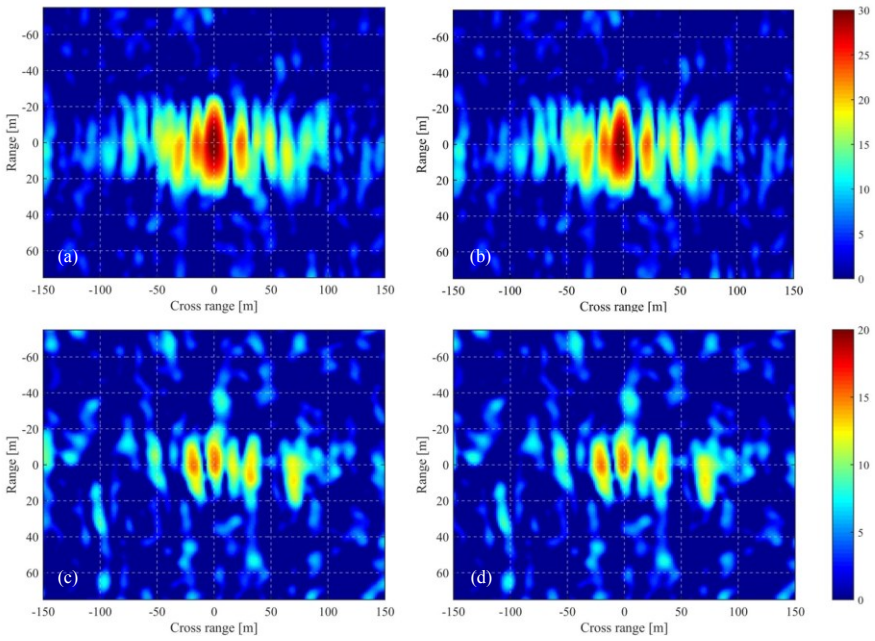

Figure 11. Monostatic range & cross-range maps images obtained for (a) sat. 1 with AIS (b) sat. 1 with MTI (c) sat. 2 with AIS (d) sat. 2 with MTI.

the analysis has been carried out separately with respect to each involved parameter (i.e., considering only one parameter at the time interested by an error) and jointly with respect to all the involved parameters (i.e., introducing random errors on all parameters in each run). As evident, for both the considered geometries (namely sat. 1 and sat. 2), the estimated scaling parameter is almost unbiased in the radial case while a bias up to 3% (for the considered error variance range), and increasing linearly with increasing inaccuracy, is observed in the cross-range motion case. Results in Table III highlight that this bias is basically due to the errors in the knowledge of the direction of motion and, particularly, it could be proven arising from the first two terms in (17). Concerning the accuracy (i.e. standard deviation), we observe a slightly variant behavior with the considered geometry (i.e. with the considered satellite); in all cases range scaling appears more robust than cross-range scaling: the worst case is equal to 0.03 in range and 0.18 in cross-range. For this last case, it could be proven that the performance appears more sensitive with respect to the target motion direction and to rotation rate and more robust with respect to the remaining parameters. In all cases the performance degradation is contained provided that the target kinematic parameters are estimated with acceptable accuracy.

It should be pointed out that, as for the results in Figure 9, different colorscales have been used also for images shown in Figure 11, due to the different levels of observed SNR. Actually, the lower level of SNR observed when sat. 2 is exploited makes this perspective less suitable for the imaging task. It fact, it can be observed the lower dynamic ranges of the IC curves for both the analyzed motion conditions (Figure 10 and Figure 12), making the estimation of the best value of Doppler rate for the target re-focusing less accurate. Moreover, the evaluation of the energy spread in the scaled range/cross-range domain is inevitably less accurate for weak target images, because it is difficult to extract the pixels belonging to the target from the

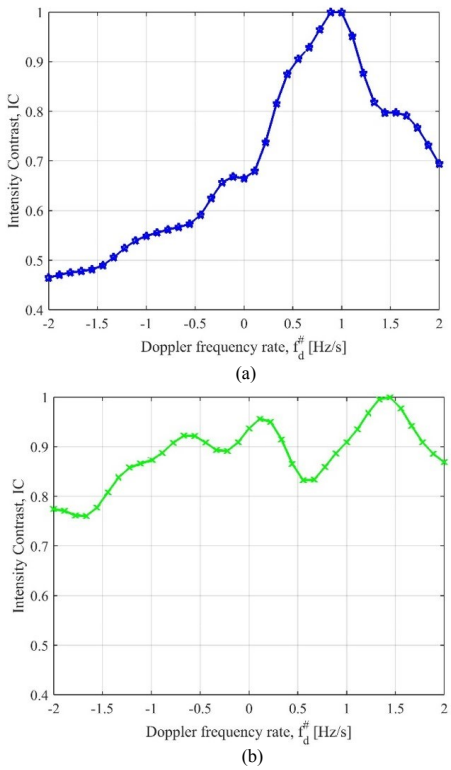

Figure 12. Intensity contrast as a function of the Doppler rate for sat.1 (a) and sat. 2 (b) in the case of a dominant tangential motion.

surrounding area [40]. Consequently, only part of the available perspectives, e.g. the ones with the highest peak power or contrast, may be fruitfully exploited for the imaging and feature extraction procedure. In this regard, it is worth to note that the exploitation of navigation satellites as opportunistic illuminators guarantees a large number of widely separated perspectives. Multistatic acquisitions therefore improve the

Table II Range scaling performance under non ideal conditions

Sat. 1	$\eta_{\phi_{Tg}}$				
	0.02	**0.04**	**0.06**	**0.08**	**0.10**
Mean value	-0.0000	-0.0000	0.0001	0.0001	0.0000
Standard deviation	0.0073	0.0144	0.0218	0.0289	0.0362

Sat. 2	$\eta_{\phi_{Tg}}$				
	0.02	**0.04**	**0.06**	**0.08**	**0.10**
Mean value	-0.0000	-0.0000	0.0000	0.0000	-0.0000
Standard deviation	0.0046	0.0092	0.0138	0.0184	0.0230

Table III Cross range scaling performance under non ideal conditions

	Sat. 1	η_γ				
		0.02	**0.04**	**0.06**	**0.08**	**0.10**
$\gamma \equiv R_R$	**Mean value**	0.0001	0.0003	0.0006	0.0012	0.0019
	Standard deviation	0.0038	0.0077	0.0116	0.0157	0.0199
$\gamma \equiv \phi_T$	**Mean value**	0.0000	-0.0001	-0.0000	-0.0001	-0.0001
	Standard deviation	0.0036	0.0073	0.0109	0.0146	0.0182
$\gamma \equiv \theta$	**Mean value**	-0.0011	-0.0043	-0.0096	-0.0165	-0.0258
	Standard deviation	0.0222	0.0439	0.0651	0.0854	0.1052
$\gamma \equiv V$	**Mean value**	-0.0000	0.0000	-0.0000	0.0000	-0.0000
	Standard deviation	0.0038	0.0076	0.0114	0.0153	0.0191
$\gamma \equiv \omega$	**Mean value**	-0.0001	0.0000	0.0002	-0.0005	-0.0002
	Standard deviation	0.0162	0.0325	0.0485	0.0647	0.0808
All param.	**Mean value**	-0.0013	-0.0050	-0.0113	-0.0202	-0.0319
	Standard deviation	0.0311	0.0623	0.0927	0.1230	0.1527

Sat. 2	η_γ				
	0.02	**0.04**	**0.06**	**0.08**	**0.10**
Mean value	0.0001	0.0003	0.0007	0.0013	0.0021
Standard deviation	0.0042	0.0085	0.0129	0.0174	0.0221
Mean value	0.0000	-0.0001	-0.0001	-0.0001	-0.0001
Standard deviation	0.0040	0.0081	0.0121	0.0162	0.0202
Mean value	-0.0011	-0.0042	-0.0094	-0.0158	-0.0249
Standard deviation	0.0326	0.0644	0.0953	0.1245	0.1523
Mean value	-0.0000	0.0000	-0.0000	0.0000	-0.0000
Standard deviation	0.0042	0.0085	0.0127	0.0170	0.0212
Mean value	-0.0001	0.0000	0.0002	-0.0005	-0.0002
Standard deviation	0.0157	0.0316	0.0473	0.0630	0.0787
Mean value	-0.0012	-0.0049	-0.0106	-0.0194	-0.0315
Standard deviation	0.0381	0.0759	0.1125	0.1483	0.1827

chance to intercept a favorable bistatic angle [26], under which the target can show nice characteristics in terms of the resulting image quality. Moreover, imaging products with further enhanced quality could also be obtained, in theory, by jointly exploiting this angular diversity by means of multistatic techniques.

Considering the favorable conditions, in the remainder of the section we will focus on sat. 1. So far, we did show results when a single frame has been exploited. As explained in Section III, given the low-resolution characteristics of the achievable images, images obtained over consecutive frames can be combined into an individual multi-frame image, so that the target shape can be more accurately reconstructed by merging the possibly different scattering centers observed over consecutive time frames. Therefore, here we considered N = 5 frames to be combined to form the multi-frame image, see Figure 4. Re-focusing of the single-frame images according to (3) has been performed and multi-frame images (4) have been obtained.

Particularly, we selected 5 successive time windows, each of 15 sec (N=5 frames, each frame with T_f=3 sec), being each window start time shifted by 3 sec with respect to the previous one. The corresponding multi-frame images, after the scaling procedure, are shown in Figure 13 (b), superimposed to the optical photograph of the ferry. For comparison, Figure 13 (a) shows the single frame images taken at the same image times. Two main comments are relevant here. (i) Although this cannot be considered a precise procedure for comparing optical and radar images, it is interesting to note how a rough correspondence between ship structure and radar images can be observed (looking for example at the funnel nicely corresponding to the brightest spots in the series of images). (ii) It is important to underline that, even though it is premature at this stage of research claiming a punctual correspondence between vessel components and image pixels, the behavior of the radar response is quite well maintained over the time. This suggests that the fruitful extraction of extra information from the images (as its length addressed in this paper) can be possible, potentially enhancing the classification capability of the system.

The reader should note that the comments above better apply to the images obtained by multiple frames. Indeed, the proper integration of multiple frame images allows increasing the contrast of the final image. The more stable scattering centers, which are expected to carry most of the information pertaining

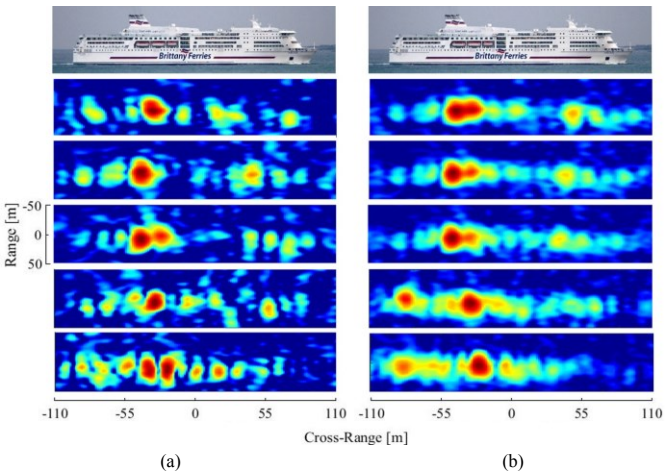

Figure 13. Single frame (a) and multi-frame (b) images – comparison with the target optical photograph.

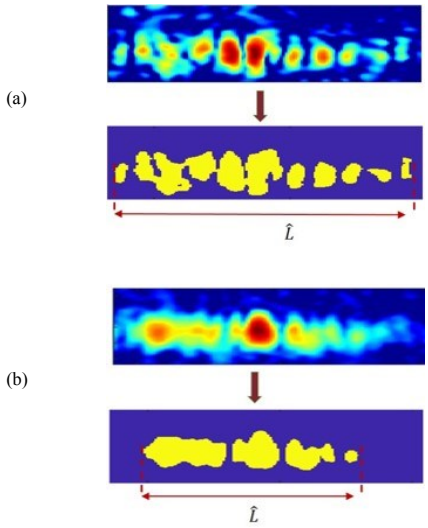

Figure 14. Single frame (a) and multi-frame (b) segmented images (η: $P_{fa} = 10^{-2}$, with clustering).

the target structure, can be effectively integrated over the different frames; at the same time spurious peaks of intensity, likely vanishing over the whole imaging interval, can be suppressed. Consequently, an easier segmentation procedure can be expected when multi-frame images are exploited.

Figure 14 shows the comparison of the application of the segmentation procedure described in Section III.C against single/multi-frame images taken at the same image time. Concerning the value to be employed for the detection threshold, it is worth to point out that ships end-points (bow and stern) usually show lower intensity [41]. Therefore, a higher threshold will likely exclude the target extremities, resulting in a smaller estimated length, whereas low thresholds might produce image regions not belonging to the ships likely carrying to over-estimations of its length. Because of the lower fluctuations of the background achieved in the multi-frame case, the method is expected having a higher capability to correctly extract the endpoints. In this case study, threshold has been set to obtain a false alarm rate equal to 10^{-2}, followed by a clustering stage to reject the isolated peaks.

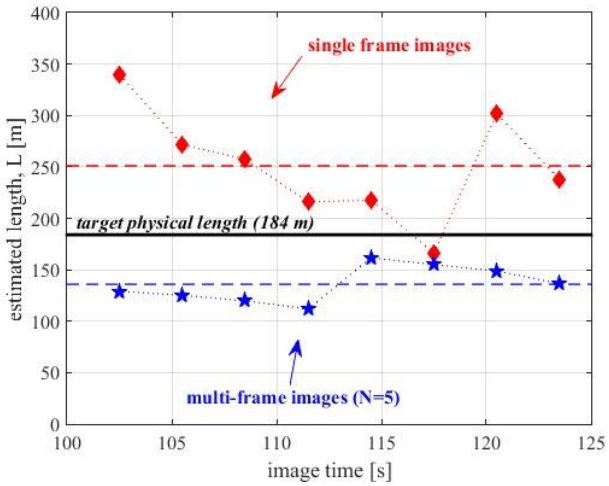

Figure 15. Estimated length.

As final result, Figure 15 shows the resulting estimated lengths using both the single frame and multi-frame images. As expected, the value obtained against the single-frame images shows strong fluctuations over the different image times, in many cases significantly overestimating the ship length. The estimation performed against the multi-frame images shows a much more stable trend and therefore is more suitable for a reliable target length measure. Finally, it should be noted that the average value obtained in the multi-frame case is of about 150 m, therefore not so far from the actual target physical length, also considering that what we are measuring is actually an electro-magnetic length, likely shorter than the physical dimension.

V. CONCLUSIONS

This work explored the use of GNSS signals for passive radar imagery of ships, as an additional capability to ship detection and localization. To this goal, we developed an appropriate processing chain to focus the images in the bistatic range & Doppler domain and define a mathematical framework suitable at translating the target occupancy in the bistatic range & Doppler domain into ship length. The conceived scheme is intended to operate in the unfavourable power budget conditions imposed by navigation satellites and therefore it takes into account the possibility to considerably extend the processing interval.

The effectiveness of the approach has been verified against experimental data involving a target of opportunity undergoing different motion conditions. Despite the limitations imposed by the restricted power budget and resolution, meaningful radar images have been obtained. By means of straightforward methods to extract the ship length from the images, we observed that the proposed approach is effectively able at estimating the target size, which is a strategic information for target classification procedure. It has also been observed that the focused images show a quite stable behaviour when taken over different image times, also showing a nice correlation with the target shape. These results encourage at spending more efforts

in this topic, for even more information about the target characteristics could be inferred from the images.

The next stage of research is exploring the multistatic imagery case. Particularly, the natural continuation of this work is defining proper combination strategies of the images obtained from multiple baselines in order to achieve a multistatic image product with improved quality. Moreover, variations of the radar signatures under multiple illumination angles could be exploited to gain extra information about the target characteristics. Overall, the multiple and widely separated perspectives simultaneously available in the GNSS-based multistatic radar system could allow alleviating the shortcomings deriving from the restricted signal power and bandwidth, enhancing the target information space and potentially enabling finer classification strategies.

REFERENCES

[1] M. Martin-Neira, "A passive reflectometry and interferometry system (PARIS): Application to ocean altimetry," *Ecol. Soc. Amer. J*., vol. 17, no 4, pp. 331-355, Dec. 1993.

[2] S. Jin, G. P. Feng, and S. Gleason, "Remote sensing using GNSS signals: Current status and future directions," *Adv. Space Res*., vol. 47, no. 10, pp. 1645–1653, May 2011.

[3] V. U. Zavorotny, S. Gleason, E. Cardellach, and A. Camps, "Tutorial on Remote Sensing Using GNSS Bistatic Radar of Opportunity," *IEEE Geosci. Remote Sens. Mag.*, vol. 2, no. 4, pp. 8-45, Dec. 2014.

[4] J. Mashburn, P. Axelrad, S. T. Lowe and K. M. Larson, "Global Ocean Altimetry With GNSS Reflections From TechDemoSat-1," *IEEE Trans. Geosci. Remote Sens*, vol. 56, no. 7, pp. 4088-4097, July 2018.

[5] F. Huang et al., "Sequential Processing of GNSS-R Delay-Doppler Maps to Estimate the Ocean Surface Wind Field," *IEEE Trans. Geosci. Remote Sens.,* in press.

[6] M. Antoniou, M. Cherniakov, GNSS-based passive SAR, in *Novel Radar Techniques and Applications*, R. Klemm *et al*., Eds., London, UK: The Institution of Engineering and Technology, 2018.

[7] H. Ma, M. Antoniou, and M. Cherniakov, "Passive GNSS-based SAR resolution improvement using joint Galileo E5 signals," *IEEE Geosci. Remote Sens. Lett*., vol. 12, no. 8, pp. 1640–1644, Aug. 2015.

[8] F. Liu, M. Antoniou, Z. Zeng, and M. Cherniakov, "Coherent change detection using passive GNSS-based BSAR: Experimental proof of concept," *IEEE Trans. Geosci. Remote Sens*., vol. 51, no. 8, pp. 4544–4555, Aug. 2013.

[9] Q. Zhang, M. Antoniou, W. Chang, and M. Cherniakov, "Spatial decorrelation in GNSS-based SAR coherent change detection," *IEEE Trans. Geosci. Remote Sens*., vol. 53, no. 1, pp. 219-228, Jan. 2015.

[10] F. Liu, X. Fan, T. Zhang and Q. Liu, "GNSS-Based SAR Interferometry for 3-D Deformation Retrieval: Algorithms and Feasibility Study," *IEEE Trans. Geosci. Remote Sens*, vol. 56, no. 10, pp. 5736-5748, Oct. 2018.

[11] F. Santi, M. Antoniou, D. Pastina, "Point spread function analysis for GNSS-based multistatic SAR," *IEEE Geosci. Remote Sens. Lett*., vol. 12, no. 2, pp. 304-308, Feb. 2015.

[12] T. Zeng *et al*., "Multiangle BSAR Imaging Based on BeiDou-2 Navigation Satellite System: Experiments and Preliminary Results," *IEEE Trans. Geosci. Remote Sens*, vol. 53, no. 10, pp. 5760-5773, Oct. 2015.

[13] F. Santi, M. Bucciarelli, D. Pastina, M. Antoniou, M. Cherniakov, "Spatial resolution improvement in GNSS-based SAR using multistatic acquisition and feature extraction," *IEEE Trans. Geosci. Remote Sens.*, vol. 54, no. 10, pp. 6217-6231, Oct. 2016.

[14] U. Nithirochananont, M. Antoniou, M. Cherniakov, "Passive multistatic SAR - experimental results", *IET Radar Sonar Nav*., vol. 13, no. 2, pp. 222-228, Nov. 2018.

[15] E. P. Glennon, A. G. Dempster, C. Rizos, "Feasibility of air target detection using GPS as a bistatic radar," *J. Global Positioning Syst*., vol. 5, no. 1-2, pp. 119-126, 2006.

[16] V. Kock and R. Westphal, "New approach to a multistatic passive radar for air/space defense," *IEEE Aerosp. Electron. Syst. Mag*., vol. 10, no. 11, pp. 24-32, Nov. 1995.

[17] I. Suberviola, I. Mayordomo, and J. Mendizabal, "Experimental results of air target detection with a GPS forward scattering radar," *IEEE Geosci. Remote Sens. Lett*., vol. 9, no. 1, pp. 47-51, Jan. 2012.

[18] C. Hu, C. Liu, R. Wang, L. Chen, L. Wang, "Detection and SISAR Imaging of Aircrafts Using GNSS Forward Scatter Radar: Signal Modeling and Experimental Validation", *IEEE Trans. Aerosp. Electron. Syst*., vol. 53, no. 4, pp. 2077-2093, Aug. 2017.

[19] C. V. Ilioudis *et al*., "GNSS Based Passive Radar for UAV Monitoring," *2019 IEEE Radar Conference (RadarConf)*, Boston, MA, USA, 2019, pp. 1-6

[20] M.-P. Clarizia, P. Braca, C. S. Ruf, and P. Willet, "Target detection using GPS signals of opportunity," *Int. Conf. Information Fusion*, Washington, DC, July 2015.

[21] A. Di Simone, H. Park, D. Riccio, and A. Camps, "Sea target detection using spaceborne GNSS-R delay-Doppler maps: Theory and experimental proof of concept using TDS-1 data," *IEEE J. Sel. Top. Appl. Earth Obs. Remote Sens*., vol. 10, no. 9, pp. 4237-4255, Sep. 2017.

[22] A. Di Simone, et al., "Spaceborne GNSS-Reflectometry for Ship-Detection Applications: Impact of Acquisition Geometry and Polarization," *IGARSS 2018 - 2018 IEEE International Geoscience and Remote Sensing Symposium*, Valencia, 2018, pp. 1071-1074.

[23] H. Ma, M. Antoniou, D. Pastina, *et al*., "Maritime moving target indication using passive GNSS-based bistatic radar," *IEEE Trans. Aerosp. Elec. Syst*., vol. 54, no. 1, pp-115-130, Feb. 2018.

[24] D. Pastina, F. Santi, F. Pieralice, *et al*., "Maritime moving target long time integration for GNSS-based passive bistatic radar," *IEEE Trans. Aerosp. Elec. Syst*., vol. 54, no. 6, pp. 3060-3083, Dec. 2018.

[25] H. Ma, M. Antoniou, A.G. Stove, J. Winkel, and M. Cherniakov, "Maritime moving target localization using passive GNSS-based multistatic radar," *IEEE Trans. Geosci. Remote Sens*., vol. 56, no. 8, pp. 4808-4819, Aug. 2018.

[26] F. Santi, F. Pieralice, D. Pastina, "Joint detection and localization of vessels at sea with a GNSS-based multistatic radar," *IEEE Trans. Geosci. Remote Sens.*, vol. 57, no. 8, pp. 5894 - 5913, Aug. 2019.

[27] D. Olivadese, E. Giusti, M. Martorella, A. Capria, and F. Berizzi, "Passive ISAR with DVB-T signals," *IEEE Trans. Geosci. Remote Sens*., vol. 51, no. 8, pp. 4508-4517, Aug. 2013.

[28] D. Pastina, M. Sedehi and D. Cristallini, "Passive bistatic ISAR based on geostationary satellites for coastal surveillance," 2010 IEEE Radar Conference, Washington, DC, 2010, pp. 865-870.

[29] Barcena-Humanes, J.-L., Del-Rey-Maestre, N., Jarabo-Amores, M.P., Mata-Moya, D., Gomez-Del-Hoyo, P., "Passive radar imaging capabilities using space-borne commercial illuminators in surveillance applications", *2015 Signal Processing Symposium (SPSympo)*, Debe, 2015, pp. 1-5.

[30] I. Pisciottano, D. Cristallini, J. Schell, and V. Seidel, "Passive ISAR for Maritime Target Imaging: Experimental Results," *Int. Radar Symp.*, Bonn, Germany, June 2018, pp. 1–10.

[31] D. Cristallini, I. Pisciottano, and H. Kuschel, "Multi-band passive radar imaging using satellite illumination," *International Conference on Radar*, Brisbane, Australia, August 2018.

[32] F. Santi, D. Pastina, "A parasitic array receiver for ISAR imaging of ship targets using a coastal radar," *Int. Journal of Antennas and Propagation*, vol. 2016, Article ID 8485305, 11 pages.

[33] F. Pieralice, F. Santi, D. Pastina, M. Antoniou, M. Cherniakov, "Ship targets feature extraction with GNSS-based passive radar via ISAR approaches: preliminary experimental results," *Proc. EUSAR 2018*, Aachen, Germany, 4-7 June 2918.

[34] F. Santi, F. Pieralice, D. Pastina, M. Antoniou, M. Cherniakov, "Passive radar imagery of ship targets by using navigation satellites transmitters of opportunity," *Proc. Int. Radar Symp. 2019*, Ulm, Germany, 26-28 June 2019.

[35] S. Herman, and P. Moulin "A particle filtering approach to FM-band passive radar tracking and automatic target recognition," in *Proc. IEEE Aerospace Conference*, Big Sky, Montana, USA, 9-16 March 2002, vol. 4, pp. 4-1789-4-1808.

[36] M. Tobias, A. D. Lanterman, "Probability Hypothesis Density-based multitarget tracking with bistatic range and Doppler observations," *IEE Proc. Radar, Sonar Nav.*, vol. 152, Issue 3, 3 Jun. 2005, pp. 195-205.

[37] F. Santi, D. Pastina, M. Bucciarelli, "Experimental Demonstration of Ship Target Detection in GNSS-Based Passive Radar Combining Target Motion Compensation and Track-before-Detect Strategies", *Sensors* 2020, 20(3), 599.

[38] V. Chen, M. Martorella, *Inverse Synthetic Aperture Radar Imaging: Principles, Algorithms and Applications*, SciTech: Edison, NJ, USA, 2014.

[39] D. Pastina, "Rotation motion estimation for high resolution ISAR and hybrid SAR/ISAR target imaging," in *Proc. IEEE Radar Conf*., Rome, Italy, May 2008, pp. 1–6.

[40] Wehner D.R.: 'High-resoultion radar' (Artech House, Boston, MA, USA, 1995, 2nd edn.)

[41] S. Musman, D. Kerr, C. Bachmann, "Automatic recognition of ISAR ship images," *IEEE Trans. Aerosp. Electron. Syst*., vol. 35, no. 4, pp. 1240–1252, Oct. 1999.

Debora Pastina (M'01) received the Laurea degree in telecommunications engineering and the Ph.D. degree in information and telecommunications engineering from Sapienza University of Rome, Rome, Italy, in 1996 and 2000, respectively.

From July 1998 to March 1999, she carried on research activity with the SAR Processing Team, Defence Evaluation Research Agency (DERA), Malvern, U.K. She is currently an Assistant Professor in the DIET Department, Sapienza University of Rome. She is involved and is responsible of scientific research projects funded by the Italian Ministry of Research, by the Italian Space Agency, by the European Commission and by the national radar industry. The results of her activity have been reported in more than 100 journal and conference papers. Her main research interests include SAR/ISAR techniques, GNSS-based passive radar systems, FSR systems and techniques, clutter models, and radar detection in non-Gaussian clutter.

Dr. Pastina was the Chairman of the Local Committee of the IEEE/ISPRS Joint Workshop Urban 2001. She was the Publication Chair of the 2008 IEEE Radar Conference. She is a member of the Editorial Board of the International Journal of Electronics and Communications (AEÜ, Elsevier) and of the IEEE TRANSACTION ON AEROSPACE AND ELECTRONIC SYSTEMS.

Fabrizio Santi (M '15) received the Master's degree (*cum laude*) in telecommunication engineering and the Ph.D. degree in remote sensing from Sapienza University of Rome, Italy, in September 2010 and June 2014, respectively.

From April to September 2013, he carried on research activity with the Microwave Integrated Systems Laboratory, University of Birmingham, U.K. He is currently a Postdoctoral Researcher with the Department of Information Engineering, Electronics and Telecommunications, Sapienza University of Rome. He is involved in scientific research projects funded by the European Commission, the Italian Space Agency and the national radar industry. The results of his research activity have been reported in a number of journals and conference papers. His main research interests include SAR/ISAR radar imaging and space-based active and passive radar systems.

Dr. Santi received the Best Italian Thesis on Remote Sensing Award from the IEEE Geoscience and Remote Sensing South Italy Chapter in 2010. He is a member of the Editorial Board of the International Journal of Electronics and Communications (AEÜ, Elsevier) and Topic Editor of the journal Remote Sensing.

Federica Pieralice received her M. Sc. degree in aerospace engineering from Sapienza University of Rome, Italy, in 2015 with a thesis on change detection techniques for multitemporal SAR images. In February 2019 she received the Ph.D. degree in Radar and Remote sensing at the same university with a thesis on GNSS-based passive radar systems for maritime surveillance applications. During her Ph.D., she was involved in the Horizon 2020 Research Project "Galileo-based passive radar system for maritime surveillance (spyGLASS)."

In December 2019 she joined e-GEOS S.p.A, Rome, Italy, in Radar Applications Group.

Michail Antoniou, SMIEE received the B.Eng (Hons) degree in Electronic and Communications Engineering and the Ph.D degree in radar sensors and systems from the University of Birmingham, UK, in 2003 and 2007, respectively.

From 2006 to 2011 he was a Research Fellow at the Microwave Integrated Systems Laboratory, University of Birmingham, UK. Since 2011 he has been with the Department of Electronic, Electrical and Systems Engineering at the University of Birmingham, where he is currently a Reader in RF Sensing Systems. He leads a team of researchers on radar systems and signal processing, including passive radar, SAR processing, multi-static, MIMO and cognitive radar, where he has more than 100 publications in peer reviewed international journals and conferences. He has led research grants funded by the European Commission, the European Space Agency, the UK MoD and the British Council, as well as direct industrial grants in those areas.

Prof **Mike Cherniakov**, PhD, DSc, Chair in Aerospace and Electronic Systems at the UoB has 45 years of experience in radar R&D. Starting his carrier in Moscow Technical University – MIET he was founded head of Radar Laboratory with ~50 full time research staff. In 1994 he was a visiting professor in Cambridge University and from 1995 till 2000 he was with the University of Queensland, Australia. During this period, he co-founded "GroundProbe" Ltd which is now the biggest radar company in Australia with multiple divisions around the world. In 2000 he joined University of Birmingham, UK where he founded Microwave Integrated Systems Laboratory (MISL) with about 25 researches working now in various areas of radar and remote sensing. In 2016-19 he was the founded Chair of Electromagnetic Systems Interest Group (EMSIG) – UK Radar Society. In 2017 he was the first scientist awarded Christian Hülsmeyer prize for his activity in radar R&D. He is the author of more than 300 publications and editor/author of 3 books.